

Negative-ion resonances and cusps in $4^{1,3}P$ electron excitation functions of the zinc atom

S. A. Napier, D. Cvejanović, J. F. Williams, and L. Pravica

*Centre for Atomic Molecular and Surface Physics, ARC Centre for Antimatter-Matter Studies, Physics Department,
University of Western Australia, Perth 6009, Australia*

(Received 24 September 2009; published 4 March 2010)

Negative-ion resonance structures, cusps, and possibly broad shape resonances were observed in the electron impact excitation of the $4s4p^1P_1$ and $4s4p^3P_{0,1,2}$ states of zinc near the thresholds of the lowest autoionizing states. Angle differential scattered electron excitation functions show strong contributions from the decay of negative-ion resonances built on a $3d$ excited ion core with final state spin-dependent decay. Most resonances have a $3d^9ns^24p^2$ electron configuration, and they appear in one or both of the 1P_1 and $^3P_{0,1,2}$ states but with different branching ratios and angular behaviors.

DOI: [10.1103/PhysRevA.81.032701](https://doi.org/10.1103/PhysRevA.81.032701)

PACS number(s): 34.80.Dp

I. INTRODUCTION

The fundamental nature of electronic correlations in atoms became known through quantities such as the bonding energies, lifetimes, transitions rates, electronic coupling schemes, and multipole moments [1,2]. Further details emerged through observations and calculations of the anisotropy of the density and velocity distributions of electrons in an atom and their perturbations by an incoming probing particle, such as emerged through components of the tensor polarizability and related parameters [3].

Technological advances enabled fine details to be observed, as in scattering dynamics for excitation processes through angular and polarization correlations between energy loss electrons and decay fluorescence [4] and their spin dependence [5] to determine components of the tensor polarizability. Other studies concentrated on electron-pair angular correlations in ionization processes to determine effectively aspects of the spectral density profile [6]. A more revealing study of electron-electron correlations emerged from doubly excited states, such as in helium [7], which gave evidence of their consequences for asymmetric autoionization rates of different electronic series as well as asymmetric fluorescence decay rates. They showed, for example, that a fluorescent transition of an inner electron could be more probable than autoionization, at least for high principal quantum number n in a Rydberg series, when the average interelectron separation became large. In particular, for the $2pnd^1P$ series fluorescence was more probable than autoionization. For higher values of n when the Rydberg electron moves further from the nucleus, the inner electron-to-core fine-structure interaction becomes stronger than the Coulomb interaction with the outer electron, and jK coupling becomes apparent rather than LS coupling. Our research [8] pursues the competition between the autoionization and excitation processes.

We selected zinc ($Z = 30$) with the closed-shell ground-state electronic configuration $[\text{Ar}]3d^{10}4s^2$ for initial studies because the valence and subvalence excited states of the various charged states are well separated from the ground states and their spectra range from the very strong and complex open- $3d$ -shell transition metals to the relatively weak and simple closed $4s$ shell of neutral zinc. Our initial studies [9] of the integrated Stokes parameters of the 636.2-nm photons

from the excited $3d^{10}4s4d^1D_2$ state of neutral zinc atoms have shown two resonances, one at 10.98 eV with clear spin-orbit interaction and a second at 11.33 eV showing negligible spin-orbit interaction effects. Similarly [8], photons from the $4p^{1,3}P$, the $4d$, $5d$, $6d^3D_{1,2,3}$, and also the $4d$, $5d^1D_2$ states showed $3d$ core-excited negative-ion resonances between 10.5 and 11.5 eV and strong post collision interaction (PCI) effects above 11.5 eV.

The present paper concerns the excitation in the same energy region around 11 eV where the inner shell d electrons can be excited into states just above the ionization threshold where both electron correlation and relaxation effects are strong. There is competition between the excitation of autoionizing states and discrete excitation. The core-excited d states may decay by autoionization or by PCI into the higher states of a true discrete spectrum. The interaction between the discrete transitions and the continua can be quantified, at least in principle, by the variations in the shape and symmetry of the profiles of resonances and the PCI effect.

Early studies concerned photon absorption [10] from the ground state of zinc to autoionizing $J = 1$ levels of odd-parity configurations and electron-impact excitation [11] of the “optically forbidden” levels of even-parity configurations as well as levels of odd parity with $J \neq 1$. The significance of electron correlations in those studies was indicated, for example, by Cowan and Wilson [12] and Mansfield and Connerade [13] and Mansfield [14], with consideration of the interactions of the configurations of the initial ground $3d^{10}4s^2$ state, excited $3d^{10}4lnl'$ and $3d^94s^2nl$ states, the final ionic $3d^94lnl'$ states, and related shake-up and shake-off processes.

We study the special situation where the $4s$ valence and the $3d$ core electrons of the ground state with the electronic configuration $3d^{10}4s^2$ may be perturbed by low-energy incident electrons. Zinc atoms are used because of their position in the periodic table of elements where the average radial probability electron density of the $3d$ orbital becomes similar to the valence $4s$ orbital. Electron-impact excitation is used because, at energies near the thresholds for excitation of a core $3d$ electron, short-lived negative ions and autoionizing states are influenced strongly by electron correlations, as seen in PCI effects [8].

The influence of spin-orbit and electron exchange effects on electron correlations in atoms appears in many ways and can be inferred from energy levels and decay schemes. The sensitivity of spin-orbit-activated interchannel coupling in the near threshold region of a $4d$ and $3d$ subshells to show electron coupling effects has been reported recently in the energy dependence of the photoionization parameters for the final continuum states of Xe (and Rn but for $5d$) [15], Cs [16], and Ba [17] atoms. Our work aimed to observe similar possible effects of interchannel coupling by looking at the formation and decay channels of negative ions and the associated influence of spin-orbit and exchange interactions.

Our previous studies of negative-ion resonances of zinc observed their energies, assignments, and different decay channels in the 10–12 eV autoionizing region [8,18,19] and used spin-polarized electrons [9] to disentangle the role of the spin-orbit and exchange interactions for limited scattering conditions. Those studies are complemented by the present observations of the angular distribution of electrons autodeattached in the decay of negative ions into $^{1,3}P$ excited states. For those decay channels the resonances are not well separated compared to their natural width, so a partial-wave analysis of the angular electron excitation spectra was not appropriate. A comparative study of angular behavior of separated $^{1,3}P$ scattering channels with elastic scattering [19] has been made to characterize the resonance decay modes.

II. EXPERIMENT

The present, and several previous studies, used a crossed electron and atom beam apparatus to characterize electron scattering from zinc atoms. Previous studies included detection and polarization analysis of decay photons [8,20,21] and also angle differential elastically scattered electron detection [19]. Here the energy of electrons scattered at a given angle was measured and the electrons with an energy loss specific for excitation of $^{3,1}P$ states were detected. Figure 1 is a schematic representation of the beam formation and particle detection apparatus showing the high-resolution electron beam, zinc vapor source, rotatable scattered electron energy analyzer with electron detector, and the system for polarization analysis and detection of decay photons. Experiments were conducted in a vacuum chamber maintained at residual gas pressure of 5×10^{-8} Torr by a turbomolecular pump.

Electrons were produced by thermionic emission from a thoriated tungsten V-shaped filament operating at 2.4 A. The emitted electrons were extracted through a 1-mm-diameter aperture, then shaped into a beam using electrostatic aperture lenses. A 35-mm-radius 127° cylindrical electrostatic monochromator selected an energy spread of the electron beam narrower than its initial thermal distribution. Two aperture lenses and a set of orthogonal pairs of beam deflectors followed the energy selector to steer and focus the beam into the interaction region 25 mm from the electron beam exit. The pass energy and the energy spread in the incident electron beam, ΔE_G , were varied according to the requirements of the particular experiment and the need of good overall data collection efficiency.

The electron analyzer [(d) in Fig. 1], designed for the low-energy scattered electrons, was mounted on a turntable

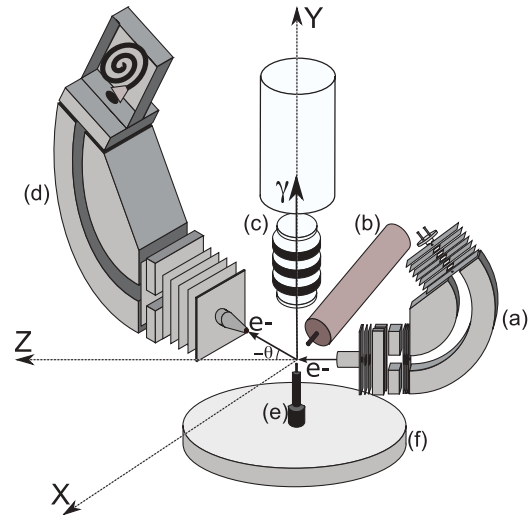


FIG. 1. (Color online) Schematic diagram of the apparatus. (a) Electron beam formation with cylindrical 127° energy selector and electron optics; (b) metal vapor source; (c) photon optics followed by photomultiplier; (d) scattered electron energy analyzer with cylindrical 127° energy selector and channel electron multiplier; (e) gas jet; (f) liquid-nitrogen-cooled copper plate.

to detect electrons at scattering angles from 0° to 110° . A 127° cylindrical electrostatic selector of 65 mm radius was used as the energy-dispersive element. It was preceded by a set of aperture lenses and a pair of electrostatic deflectors. A 3-mm entrance aperture, positioned 30 mm from the interaction region, and a 1-mm entrance aperture to the energy selector defined the geometrical angular acceptance of scattered electrons within $\pm 2^\circ$. The electron analyzer angle was calibrated and its angular resolution and performance were checked regularly by measuring around the deep minimum in the argon 40-eV elastic differential cross section at 68° [22].

The electron optics in both the monochromator and analyzer were constructed of similar materials. The lens elements and entrance and exit apertures were made from a 0.1-mm-thick molybdenum sheet, and the cylinders and deflection plates were made from copper.

The electrons were detected by a Photonis 719 channel electron multiplier placed directly over the exit aperture of the energy analyzer. The front and back of the electron channel multiplier were maintained at appropriate voltages using Ortec 459 bias supplies.

The metal vapor source is shown in Fig. 2. The zinc sample was contained inside a stainless steel housing [(b) on Fig. 2], from which it was isolated thermally by Macor blocks. Pellets of 99.999% purity zinc were vaporized within the main cavity of a thermally heated molybdenum oven. Molybdenum was chosen because it is not reactive to molten zinc [23] and has good thermal conductivity ($138 \text{ W m}^{-1} \text{ K}^{-1}$, approximately eight times higher than 316-grade stainless steel). A 150-mm-long nozzle, joined to the top of the oven, directed the free atoms into the interaction region, which was 7 mm from the 1-mm-inner-diameter exit tube. Tightly enclosing the oven and nozzle were copper cylinders with embedded twin-filament Thermocoax custom-made heaters with cold ends and a similar design of Thermocoax thermocouples. The

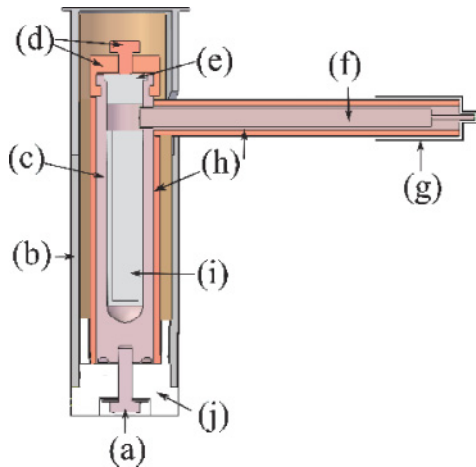


FIG. 2. (Color online) Schematic diagram of the zinc oven. (a) Stainless steel sealing screw; (b) stainless steel housing; (c) molybdenum oven; (d) copper sealing clamp; (e) molybdenum plug; (f) molybdenum-beam-forming nozzle; (g) molybdenum thermal radiation shield; (h) copper sleeves with embedded heaters; (i) cavity containing zinc pellets; (j) Macor insulation.

detection of thermal photons was decreased to a negligible amount by covering the nozzle with a molybdenum shield and coating all other potentially reflective surfaces with graphite soot.

The oven and nozzle were heated independently and the temperatures were measured using n-type thermocouples. The Thermocoax heaters and thermocouples were encapsulated in hard metal sleeving and fixed in copper cylinders to make them robust and reliable; they have never failed during the past four years. The oven temperatures varied between 480°C and 500°C to provide an adequate beam density signal, while the nozzle temperature was maintained 30°C hotter to prevent blockage of the exit tube. The zinc pellets were replenished using a resealable molybdenum plug with a copper gasket pressed onto the top of the oven.

A 20-cm-diameter, liquid-nitrogen-cooled copper plate [indicated as (f) in Fig. 1] was placed opposite the oven nozzle to collect zinc vapor and so reduce the deposition onto more sensitive parts of the apparatus. Liquid nitrogen was gravity-fed to the plate from a 6-l internal reservoir filled using an external self-pressurizing 160-l dewar. The reservoir was filled and vented via a feedthrough consisting of two $\frac{1}{4}$ -inch stainless steel pipes welded onto a $2\frac{3}{4}$ -inch Conflat flange.

A gas inlet, used for testing and optimizing the apparatus using noble gases, was centered below the target region indicated by (e) in Fig. 1. This allowed independent measurements on atomic targets in a gas phase.

The gas jet was effectively the locator of the reference axes for the scattering apparatus. The top surface of the circular plate (f) in Fig. 1 was parallel to the xz plane and the y axis was the perpendicular central axis of the plate and the central axis of the gas jet. The interaction center point was 1.5 mm above the upper end of the gas jet. The rotary tables were mounted relative to the plate (f) and rotated in the xz plane around the z axis. The incident and scattered electron analyzer and beam-forming optics were aligned by rotating them so that

a line of sight occurred through both and along two mutually perpendicular axes.

A Faraday cup (not shown in Fig. 1) was positioned 20 mm from the interaction region and used to optimize and monitor the incident electron beam. The Faraday cup consisted of a grounded 20-mm-inner-diameter copper housing terminated with 90% transparent molybdenum mesh covering the opening of an electron collection copper plate maintained at 36 V. It could be moved from outside the vacuum chamber to allow the scattered electron analyzer to approach small scattering angles.

Photons, from the target zinc atoms emitted perpendicular to the scattering plane along the positive y axis, passed through a 4-mm aperture 10 mm above the interaction region and then through a $f = 50$ mm lens placed with its focal point at the interaction region. The subsequent parallel beam of photons was transmitted through a window outside of the vacuum chamber and the wavelength selected using a narrow-band interference filter. The polarization analysis system [24] used a liquid crystal variable retarder and Meadowlark D1040 digital interface in combination with a linear polarizer and was computer controlled. Then a second $f = 100$ mm lens focused the photons onto the photocathode of an Electron Tubes 9863-350QB photomultiplier tube, which was cooled to -15°C using a EMI FACT 50 Mk III housing to reduce the dark counts typically to ~ 2 per second. All optical elements, lenses, and windows were made of UV-grade fused silica to transmit UV photons.

The output pulses from the electron and photon detectors were amplified and shaped by Ortec VT120A preamplifiers, Ortec 935 Quad Constant Fraction Discriminators, and NIM to TTL converters and counted by a data acquisition card. The incident beam current was recorded using the GPIB output of a Keithley 197A digital multimeter. A laboratory PC displayed and recorded the data and controlled the incident electron energy, electron analyzer acceptance energy, and photon polarization analysis system.

For a beam current of approximately 40 nA at 10 eV incident energy the data accumulation times varied from 4 to 36 h. The total operating time for each data set varied up to ~ 100 h, after which zinc accumulation within the apparatus often necessitated cleaning of the electron optics and insulators. Therefore a compromise was required between maximizing the energy resolution and achieving a better overall data collection efficiency by maximizing the incident electron current.

Energy calibration was obtained by detecting the 636.2-nm photons from the $4s4d^1D_2 \rightarrow 4s4p^1P_1$ transition as the incident electron energy was scanned across the steplike threshold for excitation of the $4s4d^1D_2$ state. The data were fitted to the BSRM integral cross section [25] convoluted with a Gaussian experimental apparatus function. This fit determined the full width at half maximum (FWHM) in the energy resolution of the electron beam, $\Delta E_{G,1/2}$, and the incident energy scale to within an estimated accuracy of ± 10 meV. Drifts in the incident electron energy determined from the energy calibration before and at the end of each data set accumulation were about ± 30 meV, on average.

Electron excitation functions for the singlet and triplet P states were measured by operating the spectrometer in

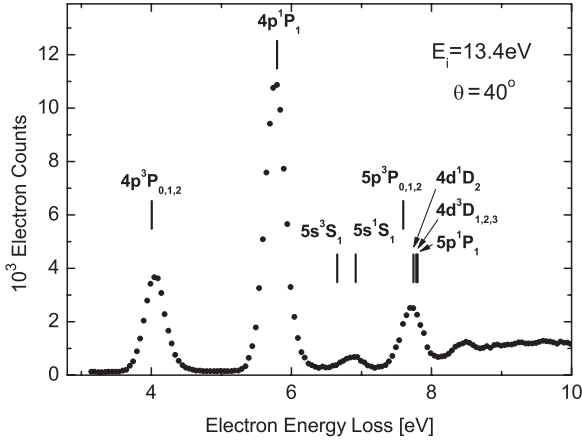


FIG. 3. Energy loss spectrum of zinc measured at incident energy of 13.4 eV and a scattering angle of 40° .

a constant-energy-loss mode. The incident electron energy and the electron analyzer acceptance energy were scanned together, with the difference between the two corresponding to the energy of an excited state. In this situation the FWHM energy resolution of the electron beam, $\Delta E_{G,1/2}$, and analyzer, $\Delta E_{A,1/2}$, combined to yield the overall resolution [26]:

$$\Delta E_{1/2} = \frac{\Delta E_{G,1/2} \Delta E_{A,1/2}}{\sqrt{\Delta E_{G,1/2}^2 + \Delta E_{A,1/2}^2}}. \quad (1)$$

A scan of the elastic scattering peak and knowledge of $\Delta E_{G,1/2}$ yielded $\Delta E_{A,1/2}$ of 100 meV and the overall resolution of the electron excitation functions was 90 meV. The performance of spectrometer was tested by observing the $^2S_{1/2}$ resonance in the angle differential cross section for elastic scattering in helium at 19.366 eV at a range of scattering angles. The dependence of the energy resolution on the operating conditions in helium was the same as in zinc and very close to theoretical predictions. Also, the overall energy resolution of the spectrometer was more than adequate to separate the electrons from the excitation of the singlet and triplet P states, as can be seen in the energy loss spectrum in Fig. 3. However, it was not sufficient to separate individual fine-structure components of the $^3P_{0,1,2}$ state.

III. RESULTS

The angle differential excitation functions for the $4p^3P_{0,1,2}$ and $4p^1P_1$ states of zinc in the vicinity of the ~ 11 eV resonances are shown in Figs. 4–8. For comparison, the data for the differential elastic scattering in the same energy region as measured by Napier *et al.* [19] on the same apparatus are shown also at each angle. For all data the negative-ion resonance shapes were determined by subtracting a least-squares polynomial fit to the slowly varying contribution to the data. This estimated non-resonance-scattered intensity is shown as a solid line together with the resulting resonance contributions as a percentage of the interpolated background. Not all the structures observed in the excitation functions in Figures 4–8 are associated necessarily with negative-ion resonances and this may be shown by a comparison of data from different measurements and different decay channels.

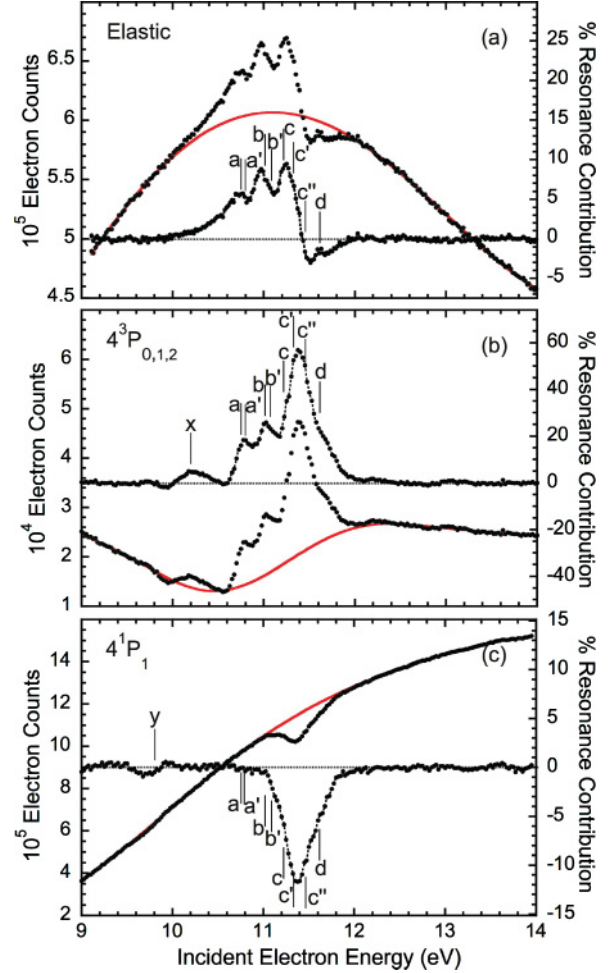


FIG. 4. (Color online) Scattered electron intensity and the percentage resonance contribution to the data measured at a scattering angle of 15° measured for (a) elastic scattering [19]; (b) excitation of the $4s4p^3P_{0,1,2}$ states; and (c) excitation of the $4s4p^1P_1$ state. The smooth solid line represents the estimated nonresonance contribution to the measured intensity. Vertical bars labeled a, a', b, b', c, c', c'', and d indicate recommended resonance energies from Ref. [19], while x and y indicate newly observed features.

For all the data the instrumental background was determined by recording the energy loss before and after the scan of each excitation function and at several energies in the relevant energy range. The background determined from the energy loss spectrum was then interpolated and subtracted from intensities measured in the corresponding excitation functions. The instrumental background for these measurements was generally low and the two states were well separated from elastic and other inelastic processes, as can be seen in the energy loss spectrum in Fig. 3 measured at an incident electron energy of 13.4 eV and a scattering angle of 40° .

The labeled vertical bars in Figs. 4–8 indicate the negative-ion resonance energies at the recommended energy values determined from our previous photon studies [8], electron transmission, and elastic scattering [19] experiments. The recommended energies for resonances a and a' and b, b' come from the electron transmission data in [19], the energy position of resonances c, c', and c'' are the average of peak energies

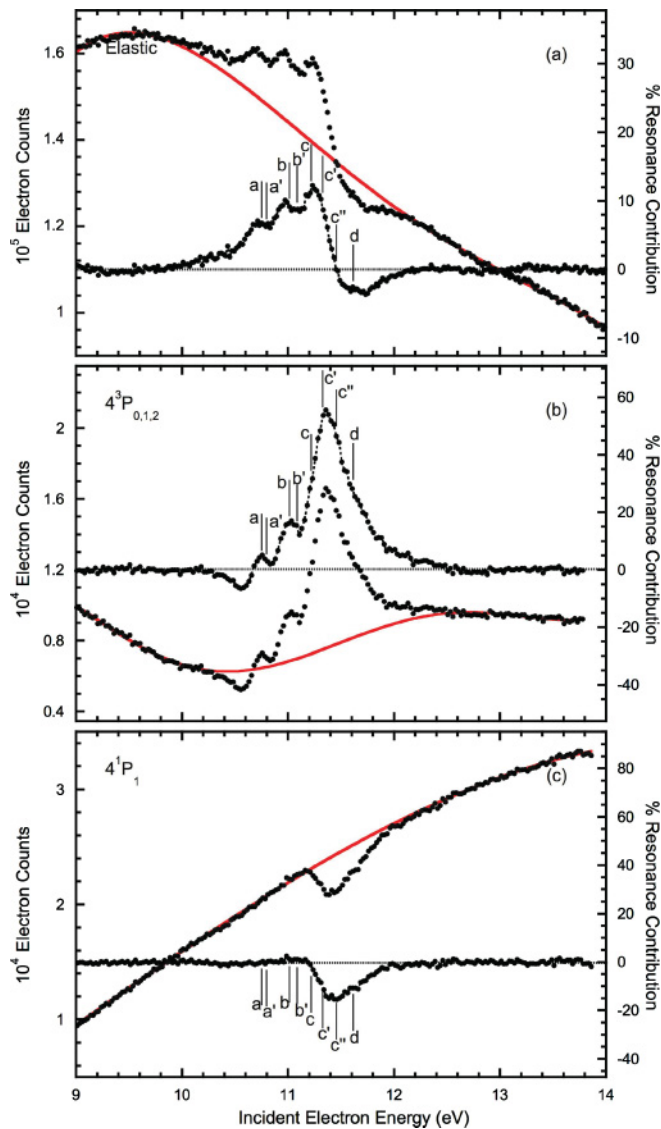


FIG. 5. (Color online) The same as Fig. 4 but for a scattering angle of 30° .

observed in photon emission [8], and the energy position of the label d comes from the peak in the differential elastic scattering signal at 15° [19].

The resonances a, a' and b, b' are well resolved only in the transmission measurements [19] while the naturally broad resonances c, c', and c'' were individually observed in photon emission from different excited states due to their selective decay. This fine structure within the three groups is not observed clearly in any of present excitation functions. The number and energies of the observed resonances are in good agreement with observations obtained from the detection of decay photons from the same states [8]. However, when comparing the results from different methods there may be important differences in the contributions of the three $J = 0, 1, 2$ fine-structure sublevels to the measured intensity for the triplet state. While photons are detected only from the $J = 1$ decay, the present electron excitation functions correspond to the unresolved contributions of all three fine-structure sublevels, which, for this spin-forbidden

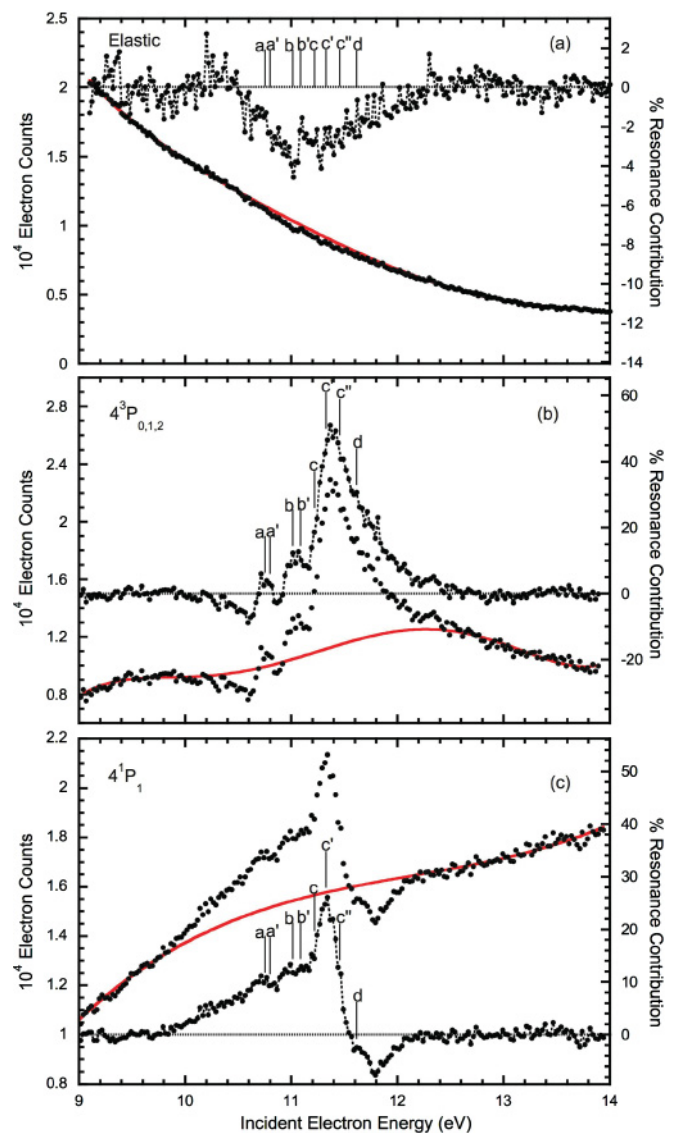


FIG. 6. (Color online) The same as Fig. 4 but for a scattering angle of 54° .

transition at low energies and in the resonance region, do not necessarily contribute in the same predictable way. Also the measured photon intensities will contain significant cascade contributions from the triplet manifold, while the electron excitation functions are free of cascade effects.

In addition to the known resonances several new structures are observed. At the scattering angle of 15° a structure marked x in Fig. 4(b) is observed in the excitation function of the $4s4p^3P_{0,1,2}$ state with a peak appearing at 10.22 eV and preceded by a shallow dip at 9.92 eV. The slope between these two structures coincides with the thresholds of the $3d^{10}4p^{2^3}P_{0,1,2}$ autoionizing states with the midpoint of the slope aligned well with the threshold of the $J = 2$ sublevel at 10.016 eV. A structure at this energy is also observed in the excitation function of the $4s4p^1P_1$ state at 90° [Fig. 7(c)]. This structure seems to be indicated with a shallow depression in the excitation function of the same state at 110° [Fig. 8(c)].

A second structure, a shallow dip, is observed also in the excitation function of the $4s4p^1P_1$ state at an energy of

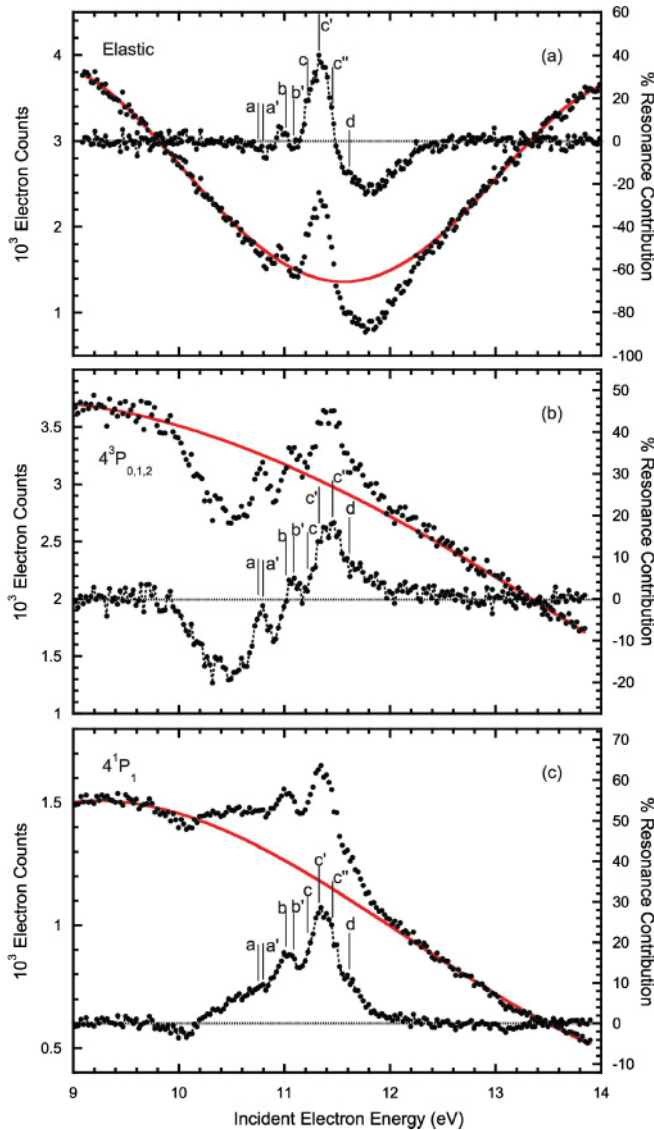


FIG. 7. (Color online) The same as Fig. 4 but for a scattering angle of 90°.

9.68 eV and 15° scattering angle [Fig. 4(c)]. The newly observed structures in the excitation functions of both the $4s4p^1P_1$ and $4s4p^3P_{0,1,2}$ states, are located either at or below the $3d^{10}4p^2$ autoionizing states, the observed 3P_J , $J = 0$ (9.940 eV), $J = 1$ (9.967 eV), and $J = 2$ (10.016 eV), and 1D_2 (predicted at 10.573 eV) [14].

At a scattering angle of 54° [Fig. 6(c)], a sharp symmetric structure is observed at 11.8 eV in the excitation function of the $4s4p^1P_1$ state. Both the shape and the energy position, coinciding with the $3d^94s^24p^3D_1$ autoionizing state threshold (11.804 eV), suggest that the structure might be a cusp on the opening of this excitation channel. A cusp is also observed at the same energy in the elastic scattering data at a scattering angle of 110° [Fig. 8(a)].

Additional broad variations of intensity are observed in all three scattering channels. Such variations are characteristic of shape resonances. The shape of these structures depends on scattering angle and differs for the three scattering channels.

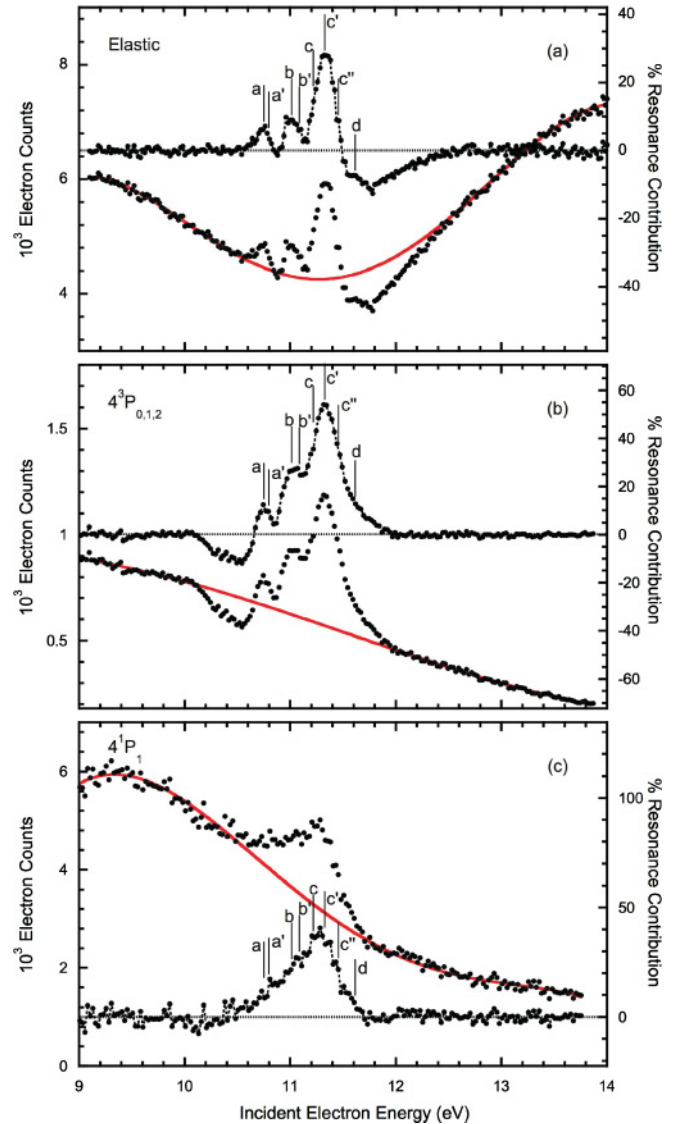


FIG. 8. (Color online) The same as Fig. 4 but for a scattering angle of 110°.

IV. DISCUSSION

The majority of the structures observed in the excitation of the $4s4p^1P_1$ and $4s4p^3P_{0,1,2}$ states in Figs. 4–8 are associated with the previously observed eight negative-ion resonances [8,19] which have been assigned a $3d^94s^24p4l$, $l = 1, 2$ electron configuration. They appear in excitation of one or both of the $^3P_{0,1,2}$ and 1P_1 states but with different branching ratios and angular behavior. To facilitate discussion of the observed angular behavior, the vertical bars on the figures corresponding to the recommended energy values [19] and Tables I and II indicate observed peak energies and the most probable association of the observed resonance structures with those reported in other types of experiments.

The most striking observation is a similarity of the resonance structures in the elastic channel and in the excitation of the triplet state. The same three resonance groups are observed in both channels. The individual resonances within each group (i.e., a, a', b, b' and c, c', c'') are not resolved due primarily to the large natural width, as evidenced from the high-resolution

TABLE I. Energies of resonance structures observed above the ionization threshold in angle differential electron excitation functions for the $4s4p^3P_{0,1,2}$ states. The total uncertainty due to energy calibration, energy drifts, and peak fitting is indicated for each structure. The letters in the top row refer to the resonance labels used to identify negative-ion resonances throughout this paper, while the second row indicates assignments proposed by [19]. All energies are in units of eV.

Angle	x $3d^{10}4p^2$	a $[^3P]^2D_{5/2}$	a' $[^3P]^2D_{3/2}$	b $[^1D]^2D_{5/2}$	b' $[^1D_{3/2}]$	c $[^1S]^2D_{5/2}$	c' $[^1S]^2D_{3/2}$	c'' $3d^94s^24p4d$	d $3d^94s^24p4d$
15°	10.18 ± 0.04	10.79 ± 0.04	–	11.02 ± 0.04	–	–	–	11.40 ± 0.03	–
30°	–	10.76 ± 0.03	–	11.04 ± 0.03	–	–	–	11.38 ± 0.04	–
54°	–	10.76 ± 0.04	–	–	11.07 ± 0.04	–	–	11.40 ± 0.03	–
90°	–	10.76 ± 0.05	–	–	11.08 ± 0.05	–	–	11.42 ± 0.04	–
110°	–	10.76 ± 0.04	–	11.03 ± 0.04	–	–	11.33 ± 0.03	–	–

transmission spectrum [19]. Consequently, the fine details within each group cannot be compared readily. In contrast, the excitation functions for the $4s4p^1P_1$ state show much less structure. At the small $\theta = 15^\circ$ and 30° and large $\theta = 110^\circ$ scattering angles, only one broad, asymmetric, structureless dip (at 15° and 30°) and peak (at 110°) is observed. Only at 54° and 90° does the excitation of the 1P_1 state show a weak contribution of the b resonance and also not convincingly the a resonance, along the dominant contribution of a narrower c' peak.

A. The $^3P_{0,1,2}$ states

In the excitation of the $4s4p^3P_{0,1,2}$ state, shown in the (b) parts of Figs. 4–8, the three resonance groups are observed clearly at all scattering angles but with different relative intensities and with what seems also different resonance contributions relative to nonresonance scattering. Even the d resonance is indicated by a shoulder in the spectrum at 15° , the only angle where it was seen clearly in elastic scattering. This d resonance is not well resolved here as it appears in the wing of the much stronger c'' resonance, which does not show an observable decay into the elastic channel at small scattering angles. At angles other than 90° , the data show strong resonance contributions of around 50% of the observed signals. At 90° , where the nonresonance intensity is also low, the resonance contributions to the excitation of the $4s4p^3P_{0,1,2}$ states were clearly at a minimum of approximately 20% of the peak. This indicates a dominant role of the p-wave electron emission in the decay process. There is however still significant structure present at 90° , indicating the presence of other partial waves.

In the excitation of the $4s4p^3P_{0,1,2}$ states, structures are observed at the energies of both the a- and b-group resonances. As a, a' and b, b' are not resolved, their individual identification and characterization based on the observed shapes and angular behavior is not straightforward. The association in Table I indicates only the predominant contribution at a particular angle. In such cases of unresolved structures a departure from the recommended values of Ref. [19] is also observed.

As indicated in Figs. 4–8, the c resonances are the dominant mechanism for resonance excitation of the triplet $P_{0,1,2}$ states. An associated strong peak is observed at all angles and is prominent especially compared to a and b resonances at $\theta = 15^\circ$, 30° , and 54° . The resonance energy determined from the peak position in a photon emission study [8] identifies the contribution to the 3P_1 excitation as a c'' resonance. At most scattering angles in the present angle differential study of the unresolved $^3P_{0,1,2}$ states, the peak seems also to fit best the energy of the resonance c'' but a contribution of the c' is also indicated by somewhat lower energies compared to the recommended values. At 110° the structure peaks at much lower values, coinciding well with c'. Also at 110° the structure is much narrower and does not have the broad high-energy tail which seems to characterize c''.

A significant difference between the relative intensities of the a-, b-, and c-group resonances in photon emission [8] and in the angle differential electron excitation functions is evident especially at small angles. In photon emission, where only the $J = 1$ state is detected, these three groups appear with not very dissimilar intensity, which is obviously not the case in the present data where the excitation of all three fine-structure sublevels is detected. One reasonable conclusion is that a large

TABLE II. Energies of resonance structures observed above the ionization threshold in angle differential electron excitation functions for the $4s4p^1P$ state. The total uncertainty due to energy calibration, energy drifts, and the peak fitting is indicated for each structure. The letters in the top row refer to the resonance labels used to identify negative-ion resonances throughout this paper, while the second row indicates assignments proposed by [19]. All energies are in units of eV.

Angle	x $3d^{10}4p^2$	a $[^3P]^2D_{5/2}$	a' $[^3P]^2D_{3/2}$	b $[^1D]^2D_{5/2}$	b' $[^1D]^2D_{3/2}$	c $[^1S]^2D_{5/2}$	c' $[^1S]^2D_{3/2}$	c'' $3d^94s^24p4d$	d $3d^94s^24p4d$
15°	–	–	–	–	–	–	11.38 ± 0.04	–	–
30°	–	–	–	–	–	–	–	11.45 ± 0.04	–
54°	–	10.74 ± 0.04	–	11.02 ± 0.05	–	–	11.32 ± 0.03	–	–
90°	10.10 ± 0.06	–	–	11.04 ± 0.04	–	–	11.36 ± 0.04	–	–
110°	–	–	–	–	–	11.26 ± 0.04	–	–	–

proportion of the intensity is due to the decay into one or both of the strongly optically forbidden $J = 0$ and $J = 2$ states. The observed difference in the relative intensities is not caused entirely by resonance decay into the $J = 0, 2$ states as an unknown small contribution to the emission from the $J = 1$ state comes via cascade population.

B. 1P_1 state

The resonance structures observed in the $4s4p^1P_1$ excitation are very different and vary with angle. The broad structureless dip observed at 15° and 30° is in best accord with the c' resonance, but the shape and the width do not seem to fit observations at, for example, 90° or in the two other scattering channels. This observation will be discussed again later in relation to assignments and other experimental evidence. No contribution from either the a or b resonances is observed clearly at these angles.

At 54° and 90° additional structure indicates an indistinguishable presence of the b, b' group and a dominant c' resonance contribution; however, at 110° only a single broad peak is observed. The a and a' resonances are not observed clearly at any of the scattering angles. This is in accord with photon excitation functions measurements [8], where the a and a' resonances are indicated only by a shoulder, which in view of the present angle differential data might have a different origin.

C. Comments on assignments

It might be significant for a future interpretation to note (a) the lack of significant structures due to the a-group resonances in excitation of the $4s4p^1P_1$ state and (b) the significant difference between the singlet and triplet counterparts. The observed difference between singlet and triplet states indicates the existence of a mechanism in the decay process which is spin selective and might favor electron exchange. A similar situation was observed in the noble gases and was discussed by Buckman and Clark [27] as a trend for decay routes to preserve the nature of the ion core.

The resonances a, a' , b, b' , c, and c' have been assigned a $3d^94s^24p^2$ and c'' and d a $3d^94s^24p4d$ electron configuration [19]; these, together with proposed symmetries, are shown in Tables I and II. The proposed assignments follow from investigations of elastic scattering and are based on a comparison with the corresponding isoelectronic $3d^94s^24p^2$ autoionizing states of the gallium atom. This model assumes that interaction of the pair of outermost electrons is strongest, resulting in the L, S momentum coupling of the pair. Three possible states, 3P , 1D , and 1S , describing this pair for the $3d^94s^24p^2$ resonance states are indicated inside the square brackets in Tables I and II. The particular state symmetries are based on the assumption that comparison with Ga is an appropriate model and also take into account restrictions imposed by conservation of symmetry in elastic scattering. For the case of inelastic scattering, because the atom is generally left in a state with nonzero angular momentum after the decay of the negative ion, the emitted electron is not restricted to a single partial wave. So, resonances with $J = 3/2$ or $5/2$ and even parity as identified from elastic scattering can decay to

the $4p^3P_{0,1,2}$ and $4p^1P_1$ states by the emission of either a p - or f -wave electron. A more detailed analysis is prevented here by the fact that different $J = 0, 1, 2$ final states are not observed separately.

Conservation of angular momentum is a less clear approach if spin flip is possible and angular momentum coupling uncertain as is the case here. Evidence from spin-polarized electron excitation of zinc indicates [9] the b and c' resonances exhibit exchange and the b resonance indicates a clear signature of spin-orbit interaction. Also our preliminary measurements of spin up/down asymmetries in spin-polarized electron scattering [28] indicate strong spin effects in the a–d resonance scattering. The new investigations using spin-polarized electrons are expected to shed light on the role and importance of different electron correlations under circumstances where different interactions, electrostatic, magnetic, and exchange have similar strengths.

An observation of additional broad structures might be important for understanding resonance scattering and properties of negative ions in the autoionizing energy region of zinc. The existence of the broad shape resonances indicated by elastic scattering seems to be supported by the excitation functions of the $4s4p^1P_1$ and $4s4p^3P_{0,1,2}$ states. The most clear evidence is presented by a broad structure centered around 10.5 eV, just below the a, a' resonance structure, in the excitation function of the $4s4p^3P_{0,1,2}$ state at 90° . As well, the extremely broad structure underlying the whole of the b–d resonance region in the excitation function of the $4s4p^1P_1$ state at 15° and 30° looks like a possible separate and broad resonance. This interpretation can then raise the possibility for interference of different overlapping resonances and their possible effects on the decay channels and angular behavior. In order to explain these and other presently available observations, the possible effects of configuration mixing and resonance formation via the $3d^94s^24p4d$ states will be explored in future work.

Future theoretical investigations are expected to shed more light on the number, assignments, and properties of negative-ion resonances in the autoionizing region of zinc and primarily on the extent, role, and the way to treat electron correlations in complex metal atoms.

V. CONCLUSION

Angle differential excitation functions of the $4s4p^3P_{0,1,2}$ and $4s4p^1P_1$ states were measured in the energy region where the decay of negative-ion resonances, formed upon the excitation of one inner $3d$ electron, affects the cross sections for excitation of neutral states. The final state spin-dependent decay of the resonances was demonstrated clearly. Most of the known resonances have strong effects on excitation of the $4s4p^3P_{0,1,2}$ states, where up to 50% of the angle differential cross section comes from resonance contributions. For resonance decay into this state there is a strong similarity with resonance elastic scattering. In contrast, the excitation of the $4s4p^1P_1$ state is affected less, both in terms of relative resonance contribution and the number of resonances decaying into this scattering channel. The shapes of the resonance profiles in the excitation of the $4s4p^1P_1$ state are different and, together with the broad structures in the elastic and

the $4s4p^3P_{0,1,2}$ channels, suggest the existence of broad, most likely shape, resonances in the same energy region. Weak structures, associated most likely with the $3d^{10}4p^2n\ell$ resonance configurations, and cusps, associated with some of the $3d^94s^24p$ autoionizing state thresholds, have been observed.

Here we present further evidence of the significance of the excitation of one inner $3d$ electron, as an intermediate step, on the excitation of neutral states of a zinc atom. A theoretical model of electron scattering with an open $3d$ core is needed to improve the interpretation of the data. Further study of a highly correlated electronic system, such as a negative ion, would

improve our understanding of the role of different interactions where there is a close balance of noncentral electrostatic, magnetic (spin orbit), and quantum exchange effects affecting momentum coupling.

ACKNOWLEDGMENTS

This work was supported by the Australian Research Council and the University of Western Australia. SN was supported by an Australian Postgraduate Award. The technical assistance of S. Key of the UWA mechanical workshop is acknowledged.

-
- [1] R. D. Cowan, *The Theory of Atomic Structure and Spectra* (University of California Press, Berkeley, Los Angeles, London, 1981).
- [2] Y. Ralchenko, A. E. Kramida, J. Reader, and N. A. T. (2008), *NIST Atomic Spectra Database*, version 3.1.5 (National Institute of Standards and Technology, Gaithersburg, MD, 2008), <http://physics.nist.gov/asd3>.
- [3] U. Fano and J. W. Cooper, *Rev. Mod. Phys.* **40**, 441 (1968).
- [4] N. Andersen and K. Bartschat, *Polarization, Alignment and Orientation in Atomic Collisions* (Springer-Verlag, New York, 2001).
- [5] G. Baum, W. Blask, and M. Streun, *J. Phys. IV (Paris)* **9**, 219 (1999).
- [6] A. Lahman-Bennani, A. Duguet, A. Grisogono, and M. Lecas, *J. Phys. B* **25**, 2873 (1992).
- [7] M. Zitnik, K. Bucar, M. Stuhec, F. Penent, R. I. Hall, and P. Lablanquie, *Phys. Rev. A* **65**, 032520 (2002).
- [8] S. A. Napier, D. Cvejanović, J. F. Williams, and L. Pravica, *Phys. Rev. A* **78**, 032706 (2008).
- [9] L. Pravica, D. Cvejanović, J. F. Williams, and S. A. Napier, *Phys. Rev. A* **75**, 030701(R) (2007).
- [10] B. Brehm and H. Pfeiffenberger-Pertl, *Z. Phys. A* **320**, 37 (1985).
- [11] C. G. Back, M. D. White, V. Pejcev, and K. J. Ross, *J. Phys. B* **14**, 1497 (1981).
- [12] R. D. Cowan and M. Wilson, *J. Phys. B* **21**, L275 (1988).
- [13] M. W. D. Mansfield and J. P. Connerade, *Proc. R. Soc. Ser. A* **359**, 389 (1978).
- [14] M. W. D. Mansfield, *J. Phys. B* **14**, 2781 (1981).
- [15] S. S. Kumar, T. Banerjee, P. C. Deshmukh, and S. T. Manson, *Phys. Rev. A* **79**, 043401 (2009).
- [16] H. Farrokhpour, M. Alagia, M. Y. Amusia, L. Avaldi, L. V. Chernysheva, M. Coreno, M. de Simone, R. Richter, S. Stranges, and M. Tabrizchi, *J. Phys. B* **39**, 765 (2006).
- [17] H. Farrokhpour *et al.*, *J. Phys. B* **40**, 4005 (2007).
- [18] S. A. Napier, D. Cvejanović, J. F. Williams, and L. Pravica, *J. Phys. B* **40**, 1323 (2007).
- [19] S. A. Napier, D. Cvejanović, P. D. Burrow, J. F. Williams, J. A. Michejda, and L. Pravica, *Phys. Rev. A* **80**, 042710 (2009).
- [20] S. A. Napier, D. Cvejanović, J. F. Williams, and L. Pravica, *Phys. Rev. A* **78**, 022702 (2008).
- [21] S. A. Napier, D. Cvejanović, J. F. Williams, L. Pravica, D. Fursa, I. Bray, O. Zatsarinny, and K. Bartschat, *Phys. Rev. A* **79**, 042702 (2009).
- [22] J. F. Williams and B. A. Willis, *J. Phys. B* **8**, 1670 (1975).
- [23] K. J. Ross and B. Sontag, *Rev. Sci. Instrum.* **66**, 4409 (1995).
- [24] J. E. Furst, D. H. Yu, P. A. Hayes, C. M. D'Souza, and J. F. Williams, *Rev. Sci. Instrum.* **67**, 3813 (1996).
- [25] O. Zatsarinny and K. Bartschat, *Phys. Rev. A* **71**, 022716 (2005).
- [26] F. H. Read, *J. Phys. B* **8**, 1034 (1975).
- [27] S. J. Buckman and C. W. Clark, *Rev. Mod. Phys.* **66**, 539 (1994).
- [28] S. A. Napier, D. Cvejanović, J. F. Williams, L. Pravica, S. N. Samarin, A. D. Sergeant, P. Guagliardo, and P. Wilkie, *J. Phys.: Conf. Ser.* **185**, 012032 (2009).